Physics in Medicine &
Biology

IPEM
Institute of Physics and Engineering in Medicine

PAPER • **OPEN ACCESS**

A procedure for accurate dose measurement in radiotherapy research at millimetre-sized synchrotron beams

To cite this article: Catharina Mewes *et al* 2025 *Phys. Med. Biol.* **70** 225015

View the article online for updates and enhancements.

You may also like

- Mesh-based detailed skeletal models for the ICRP Reference Adults: Part 1. development and dosimetric impact
Chansoo Choi, Robert J Dawson, Yitian Wang et al.
- A comprehensive dose-volume histogram-based index for radiotherapy treatment plan quality evaluation: application to breast cancer radiotherapy
Hiran CG Maladenige, Jan Seppälä, Tuomas Virén et al.
- A biophysical model of cell survival in particle beam therapy combined with hyperthermia incorporating temperature and radiation quality
Yuki Kase, Shotaro Nakahara and Yoshitaka Matsumoto

This content was downloaded from IP address 134.28.50.156 on 24/11/2025 at 08:03

IOP Publishing Phys. Med. Biol. 70 (2025) 225015 https://doi.org/10.1088/1361-6560/ae143a

Physics in Medicine & Biology

IPEM Institute of Physics and Engineering in Medicine

Check for updates

OPEN ACCESS

RECEIVED
7 February 2025

REVISED
28 August 2025

ACCEPTED FOR PUBLICATION
16 October 2025

PUBLISHED
12 November 2025

Original Content from this work may be used under the terms of the Creative Commons Attribution 4.0 licence.

Any further distribution of this work must maintain attribution to the author(s) and the title of the work, journal citation and DOI.

PAPER

A procedure for accurate dose measurement in radiotherapy research at millimetre-sized synchrotron beams

Catharina Mewes[1,*], **Michael Lerch**[2], **Marco Petasecca**[2], **Johannes Klingenberg**[3], **Guilherme Abreu Faria**[3], **Ulrich Lienert**[4], **Elisabeth Schültke**[5], **Jason Paino**[2], **James Cayley**[2], **Marie Wegner**[1,6], **Stefan Fiedler**[7] and **Elisabetta Gargioni**[1]

[1] Department of Radiotherapy and Radiation Oncology, University Medical Center Hamburg-Eppendorf (UKE), Hamburg, Germany
[2] Centre for Medical Radiation Physics (CMRP), Faculty of Engineering and Information Sciences, University of Wollongong, Wollongong, Australia
[3] Materials Physics, X-ray Diffraction with Synchrotron Radiation, Helmholtz-Zentrum hereon GmbH, Hamburg, Germany
[4] Deutsches Elektronen-Synchrotron (DESY), Hamburg, Germany
[5] Department of Radiotherapy, Rostock University Medical Center, Rostock, Germany
[6] Institute of Product Development and Mechanical Engineering Design, Hamburg University of Technology (TUHH), Hamburg, Germany
[7] European Molecular Biology Laboratory (EMBL), Hamburg Unit, c/o DESY, Hamburg, Germany
[*] Author to whom any correspondence should be addressed.

E-mail: catharina.mewes@uni-hamburg.de

Keywords: synchrotron, ultra-high dose rate radiotherapy, FLASH radiotherapy, microbeam radiation therapy (MRT), dosimetry, Monte Carlo simulation

Supplementary material for this article is available online

Abstract

Objective. Synchrotron-based spatially fractionated radiotherapy and ultra-high dose rate (UHDR) radiotherapy have been shown to better spare healthy tissue function in comparison to conventional radiotherapy, while controlling the tumour with the same efficacy. In recent years, an increasing amount of research has been carried out in these fields with promising results. However, further experiments remain essential, since the underlying mechanisms of healthy tissue preservation are not yet fully understood. The characterisation of synchrotron beamlines at the Deutsches Elektronen-Synchrotron in Hamburg represents an opportunity to increase the number of sites where pre-clinical studies could be conducted in the future. However, the beams available at this synchrotron are only a few millimetres in size and measuring absorbed dose with established detectors and dosimetry protocols represents a challenge. *Approach.* We show a procedure to accurately determine the beam dose rate under such conditions by first characterising a monochromatic beamline. After validation, and with the support of Monte Carlo simulations, the procedure is adapted to investigate a white-beam beamline, at which photon flux and mean energy can be varied with Cu absorbers. *Main results.* With the developed procedure, it is possible to measure absorbed dose at these beamlines with relative uncertainties below 10%. In particular, at the white-beam beamline, the dose rate varies between about 20 Gy s^{-1} and about 1800 Gy s^{-1}, thus offering the opportunity to carry out much-needed systematic studies. Moreover, pilot experiments with a mouse phantom demonstrate that it is possible to treat small animals with such small-sized beams by using dose-painting techniques, with an agreement between prescribed and delivered dose within ±15%. *Significance.* This work represents a first step towards the implementation of reproducible pre-clinical studies at the PETRA III synchrotron, further contributing to a transition of spatially-fractionated and UHDR radiotherapy techniques into clinical practice.

© 2025 The Author(s). Published on behalf of Institute of Physics and Engineering in Medicine by IOP Publishing Ltd

1. Introduction

The last decade of radiotherapy research was marked by a number of important technical advances, such as the establishment of highly-precise stereotactic irradiation techniques and enhanced image guidance through magnetic resonance imaging. Moreover, much attention is being devoted to understand the phenomena that are observed in radiotherapy at ultra-high dose rates (UHDRs) and in spatially fractionated radiotherapy (SFRT). It has been shown that these radiotherapy modalities reduce toxicity of normal tissue, while ensuring a similar or even higher probability of tumour control compared to conventional radiotherapy (Fukunaga *et al* 2021, Vozenin *et al* 2022). For this reason, SFRT and UHDR irradiations, if translated into the clinic, would enable the delivery of higher doses to tumors, and, in principle, higher doses per fraction than conventional radiotherapy, without increasing the risk of normal tissue toxicity (Bourhis *et al* 2019a, 2019b, Friedl *et al* 2021, Gaide *et al* 2022, Vozenin *et al* 2024).

An example of SFRT is represented by synchrotron microbeam radiation therapy (MRT), which is implemented through the insertion of a multi-slit collimator (MSC) into the quasi-parallel beam of a synchrotron beamline (Bräuer-Krisch *et al* 2009). With this method, it is possible to generate an array of several microbeams, with typical widths of 25–100 μm, spaced at centre-to-centre distancing of 100–400 μm (Bräuer-Krisch *et al* 2010). MRT is characterised by a large difference between the dose delivered in the microbeams (which is also called the *peak dose*) and that in the region between two microbeams, called the *valley dose*, with the peak-to-valley dose ratio (PVDR) being a decisive parameter to safely deliver this type of irradiation (Smyth *et al* 2016). In the last decade, several research groups performed experiments, both *in vitro* and *in vivo*, demonstrating the potential of MRT to control tumours with the same efficacy as conventional radiotherapy (Laissue *et al* 2001, Crosbie *et al* 2010, van der Sanden *et al* 2010, Priyadarshika *et al* 2011, Schültke *et al* 2017, 2021, Fernandez-Palomo *et al* 2020, Fukunaga *et al* 2021, Adam *et al* 2022).

The high brilliance available at synchrotrons ensures UHDR, thus making these x-ray beams a powerful tool for basic research in the field of radiotherapy, since the underlying biological mechanisms leading to normal-tissue sparing during SFRT or UHDR irradiations are not yet completely understood. Due to the increasing number of studies both in SFRT and UHDR radiotherapy, it is important to increase the availability of synchrotron beamlines where this type of research can be carried out. We therefore explored the opportunity to conduct research at the synchrotron PETRA III Deutsches Elektronen-Synchrotron (DESY, Hamburg). However, none of the beamlines at PETRA III is a dedicated biomedical beamline and the x-ray beams are a few millimetres in size, both in horizontal and in vertical direction, so that their dosimetric characterisation is very challenging. For comparison, at the ESRF biomedical beamline, ID17 (currently shut down), the maximum horizontal and vertical dimensions available at the beamline are 150 mm $\times$ 7 mm, while at that of the Australian Synchrotron, IMBL, they are 100 mm $\times$ 3 mm (ANSTO 2025, ESRF 2025).

We present in this work a procedure to define and verify reproducible irradiation protocols at PETRA III. To this purpose, we needed to conduct a thorough dosimetric study and modify some of the procedures commonly followed at other synchrotrons. After establishing and validating the method at a monochromatic beamline, which was used in the past for preliminary MRT studies (Al-Zeer *et al* 2022), we used the defined protocols at a white-beam beamline, where we can vary the dose rate over a wide range by increasing the attenuator thickness (Schültke *et al* 2022). This will be useful for future studies on the dose rate dependence of normal-tissue sparing effects (Vozenin *et al* 2024).

To confirm the robustness of our procedure, we employed an additively manufactured mouse phantom, thus mimicking the treatment of a small animal. This enabled us to compare prescribed and delivered dose under realistic pre-clinical settings prior to radiobiology experiments.

2. Materials and methods

In this work, we performed experiments, carried out with independently calibrated detectors, and Monte Carlo (MC) simulations. This was necessary to ensure the accuracy of our procedure. As already mentioned, to our knowledge, the available detectors were not yet used in such extreme conditions of both an UHDR and millimetre-sized fields, in horizontal as well as vertical direction. For a thorough characterisation of the beamlines, we carried out the following sets of measurements: (i) dose profiles to define field sizes with a flat top, (ii) depth dose curves in a PMMA plate phantom, (iii) dose rate for several beam configurations, (iv) loss of dose rate in the microbeams due to the presence of the MSC. After validating the MC simulation model, we calculated the variation of the PVDR for increasing depth in the phantom.

2.1. Beamlines

The PETRA III synchrotron (DESY, Hamburg, Germany) has 25 operational beamlines and a circumference of 2.3 km, storing electrons with an energy of 6 GeV and a current of 100 or 120 mA. The electron bunches are separated by 16 ns in the 480 bunch mode and by 8 ns in the 960 bunch mode, respectively. The two beamlines considered in this work are mainly used for material science studies. The first beamline, P21.2, is the monochromatic Swedish Materials Science beamline, mostly operated between 40 and 90 keV. The second, P61A, is the white-beam beamline operated by the Helmholtz–Zentrum hereon (Geesthacht, Germany).

In general, slits and stages for equipment are driven by remotely-controlled motors. In this way, the experimental stage can be translated vertically and horizontally through the beam. The stage holding the MSC, which can be moved independently, can also be rotated to ensure correct alignment. As the MSC slits are only 50 μm wide and 8 mm thick, the angular alignment needs to be performed very carefully (Ortiz *et al* 2022). The stage velocity can be adjusted to the users' requirements and set reliably between 0.1 and 30 mm s^{-1} in vertical, as well as up to 5 mm s^{-1} in horizontal direction.

2.1.1. Monochromatic beamline (P21.2)

The monochromatic beamline P21.2 was previously described by Lienert *et al* (2024) and used in the past for *in-vitro* MRT studies (Al-Zeer *et al* 2022). Here, photons are produced by a 4 m long in-vacuum undulator with a period of 21.2 mm. Even though a photon energy of 45 keV is used for most experiments, it is possible to change it, with the lowest possible energy being 37.5 keV. This corresponds to a flux optimised undulator gap of 7.095 mm.

The photon fluence rate at this beamline is about of 10^{14} photons $(\mathrm{s{\cdot}cm^2})^{-1}$ for 45 keV. During this work, we measured the fluence rate with a photodiode (Canberra Packard, Schwadorf, Austria), which was previously calibrated in the x-ray energy range provided by this beamline. The slits used for beam shaping are located at a distance of approximately 40 m downstream of the experimental stage, while further slits are available in the experimental hutch to reduce scattered radiation.

2.1.2. White-beam beamline (P61A)

The properties of the white-beam beamline P61 were recently described by Farla (2022). Briefly, the source consists of an array of ten damping wigglers, 4 m in length, each 2 m apart. To reduce the amount of low-energy photons and, therefore, heat load on beamline components, the beam has a permanent filtration of 0.3 mm diamond and 0.05 mm copper and is guided towards two experimental hutches, P61A and P61B. The energy spectrum of P61A, upstream of these filters, has been calculated via simulations (Schültke *et al* 2022) and is shown in figure 1. The mean energy, E_{mean}, calculated using equation (1), results to be 83 keV,

$$E_{\mathrm{mean}} = \frac{1}{N_{\mathrm{tot}}} \cdot \sum_{i=1}^{m} E_i \cdot N_i. \tag{1}$$

Here, N_{tot} is the total number of photons, m the number of energy bins and N_i the number of photons with energy E_i. The maximum energy considered in this work is 400 keV, as the fraction of photons with a higher energy is comparably small. For example, the number of photons with energy between 400 keV and 1 MeV is only 0.02% of the total number of photons between 0 and 400 keV. The photon fluence rate at this beamline is estimated to be in the order of $4 \cdot 10^{16}$ photons $(\mathrm{s{\cdot}cm^2})^{-1}$.

For MRT studies at the white-beam beamline P61A, we recently designed and installed a mobile biomedical insert (Schültke *et al* 2022). Briefly, two sets of tungsten carbide slits are available in the experimental hutch. These slits are 10 mm thick and flushed with nitrogen gas to reduce radiation-induced oxidation. Each slit has four blades, which can be moved independently, i.e. one pair in vertical and one pair in horizontal direction, respectively. When required, the MSC is placed downstream from the first set of slits. Three ionisation chambers (ICs) can be used for monitoring the beam along the set-up. The experimental stage is set up downstream of the second set of slits. Figure 2 depicts the biomedical insert and some details of the experimental set-up.

For filtering purposes, two triangular absorber blocks (wedges), moving against each other, can be controlled remotely to vary the absorber thickness in a continuous way between 0 mm and 100 mm. Graphite or copper can be used separately as the photon-attenuating material.

2.2. Dosimeters

In the following sections, we shortly introduce the dosimeters employed in this work in combination with PMMA cubic phantoms.

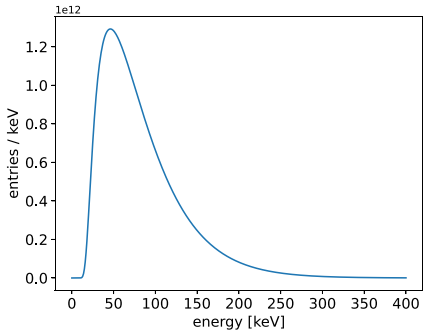

Figure 1. Simulated photon spectrum of the white-beam beamline P61A (Schültke *et al* 2022). The maximum energy considered in this work is 400 keV.

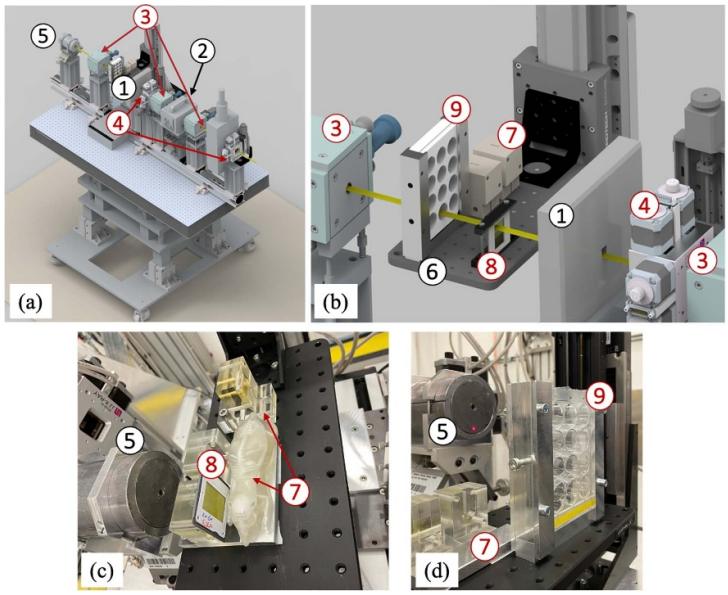

Figure 2. (a) Biomedical insert at the white-beam beamline P61A, with some details, such as incident slits (1), MSC (2), ionisation chambers (3), secondary slits (4), and beam stop (5). A zoom of the experimental area (b) depicts the experimental stage (6) with some samples, also shown in the photographs (c, d), with phantoms (7), film holder (8), and a well plate (9).

2.2.1. PTW microDiamond (MD) and soft x-ray IC

The PTW MD (TM60019) has a nominal sensitive volume of 0.004 mm^3, 2.2 mm in diameter and 1 μm in thickness and its linear response with respect to dose was found to be dose rate independent, within the experimental uncertainty, in the range 1–1000 $Gy\,s^{-1}$ (Livingstone *et al* 2016). Due to its cylindrical geometry, this detector's sensitive volume can be used with its axis both parallel (face-on orientation) and perpendicular to the beam axis (edge-on orientation, see figure 3). The MD was calibrated in face-on orientation by the manufacturer in terms of absorbed dose to water, with ^{60}Co as the reference radiation quality and has been successfully used in the past as the reference dosimeter for synchrotron-based irradiation experiments (Livingstone *et al* 2016, Davis *et al* 2021).

The PTW soft x-ray IC (34 013 W) has a sensitive volume of 5.9 mm^3 (2.9 mm in diameter and 0.9 mm in thickness). This detector was calibrated in terms of absorbed dose to water for x-ray qualities between 0.05 and 4.0 mm HVL Al, which correspond to mean photon energies between 16.4 and 36.4 keV.

2.2.2. X-Tream dosimetry system

The X-Tream dosimetry system, developed at the University of Wollongong, Australia, allows for real-time dosimetry measurements with a time resolution of one microsecond. The detector, shown in figure 4 together with the MD and the IC, consists of a single-microstrip silicon diode, 10 μm thick, fabricated on a high-resistivity epitaxial substrate, 50 μm wide (Davis *et al* 2018). The detector substrate is about 5 mm wide on each side of the detector (see also figure 4). An edge-on orientation allows

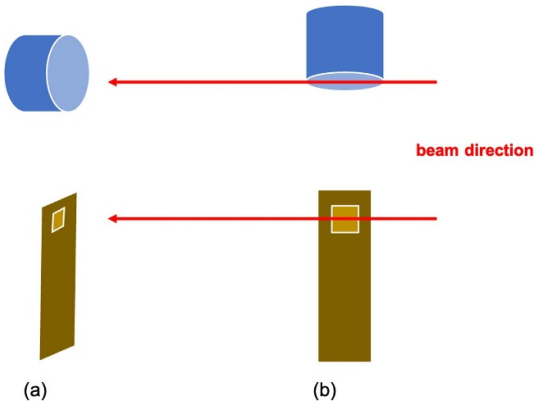

Figure 3. The two orientations that the PTW microDiamond (schematically represented in blue) and the X-Tream detector (schematically represented in brown) can have with respect to the beam. In the face-on orientation (a), the beam is incident on the surface of the sensitive volume (represented in light blue and light brown, respectively). A 90° rotation sets the dosimeters in the edge-on orientation (b).

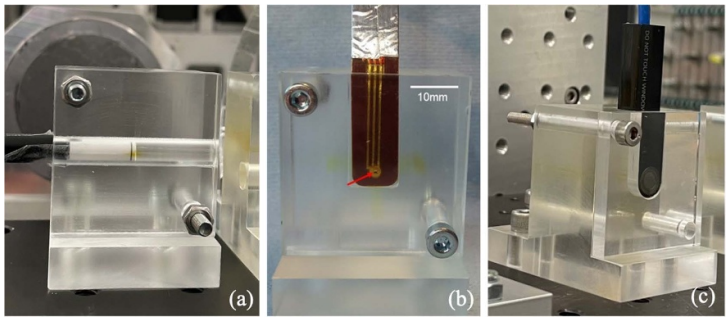

Figure 4. Set-up of the dosimeters in PMMA phantoms at the white-beam beamline P61A. (a) microDiamond in edge-on orientation, (b) X-Tream detector in face-on orientation and (c) soft x-ray ionisation chamber. The black line in (a) and the red arrow in (b) show the approximate sensitive area of the detectors. For possible detector orientations, see also figure 3.

for the highest spatial resolution (see figure 3). The detector response is linear over a wide range of dose rates (Davis *et al* 2021) and was characterised in detail for MRT dosimetry during previous studies (Petasecca *et al* 2012, Fournier *et al* 2017). During this work, the X-Tream dosimetry system was mainly used for relative dose measurements and for determining the PVDR.

2.2.3. Radiochromic films

For two-dimensional dose verifications in the broad beam (BB) configuration (i.e. without MSC), we used GafChromic^{TM} HD-V2 dosimetry films (Ashland, Wilmington, USA). According to the manufacturer, the response of these films is energy and dose rate independent, and suitable for measuring absorbed dose in the range between 10 and 1000 Gy (Ashland 2025). We calibrated the films in terms of absorbed dose to water at a medical linear accelerator (Varian TrueBeam) in the range between 10 and 350 Gy. For calibration and subsequent measurements, we scanned each film individually, seven days after irradiation, with an Epson scanner (model V850 pro) at a resolution of 350 dpi. We determined the calibration curve with common methods found in literature and according to manufacturer recommendations (Devic *et al* 2009, Chen *et al* 2016).

2.3. Procedure for accurate dose delivery

To ensure data reproducibility and reliability in radiobiology experiments, the delivered radiation dose must be known very accurately. It is therefore necessary to perform dosimetry with detectors that can be calibrated at a secondary standard laboratory in terms of absorbed dose. Both the PTW soft x-ray IC and the MD satisfy this condition. However, since the radiation fields at the investigated beamlines are a few millimetres in size, both horizontally and vertically, their dosimetric characterisation is particularly challenging.

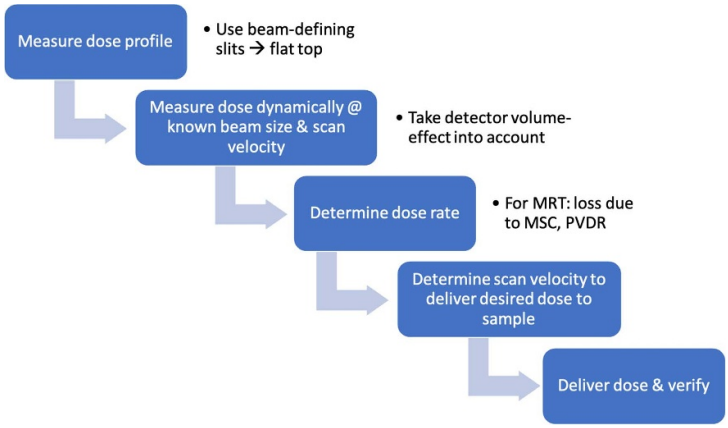

Figure 5. Procedure for accurate absorbed dose measurements and reproducible dose delivery at PETRA III beamlines that are characterised by very small beam sizes.

The methods used in literature for measuring dose at synchrotron beamlines needed, therefore, to be adapted to these extreme conditions, as explained in section 2.5, and schematically summarised in figure 5.

Briefly, we start with using beam-defining slits to obtain a flat dose profile. In this work, we consider a dose profile to be flat if the relative deviation between maximum and minimum top dose values is within ±10%. In a second step, for the given field size, we measure the absorbed dose at the reference point by translating the detector vertically through the beam and determine the beam dose rate (see section 2.5). This method is referred to as dynamic dose measurement in the following. In the case of MRT, we then assess the loss of dose rate due to the MSC, as well as the PVDR. Finally, we deliver the desired dose to a sample with the same dynamic procedure and verify it with an independent measurement, as shown in the following sections.

2.4. Beam size—measurement and definition

In order to ensure a flat horizontal (or vertical) dose profile, we optimise the position of beam-defining slits, so that we can deliver a homogeneous dose to biological samples and produce a sharp dose gradient at the field edges. In particular, we report the beam width and height as the full width at half maximum (FWHM) of dose profiles with a flat top. We measured dose profiles in the corresponding phantom, both with the MD and the X-Tream dosimetry system (see figure 4).

2.5. Dose measurements

We adapted the approach described in the literature for determining the absolute dose rate for similar set-ups (Prezado *et al* 2011, Fournier *et al* 2016, Lye *et al* 2016, Davis *et al* 2021). Briefly, the dosimeters are moved vertically through the beam at a well-defined scanning velocity, v_{scan}. If the beam height, h_{beam}, is smaller than the detector size facing the beam, the measured signal, M_Q, is then integrated along the scan length. The absorbed dose in PMMA is measured with the in-phantom method. In line with the IAEA code of practice TRS-398 (International Atomic Energy Agency 2024), we determine the absorbed dose, $D(z)$, in PMMA as:

$$D_{\mathrm{PMMA}}(z) = D_w(z') = M_Q \cdot N_{D_w,Q_0} \cdot k_{Q,Q_0} \cdot K_{f,Q}. \tag{2}$$

In equation (2), M_Q is the dosimeter reading in PMMA at the synchrotron beamline; N_{D_w,Q_0} the detector calibration factor in terms of dose to water, provided for defined radiation qualities and irradiation geometries, which are reported in the respective calibration certificates; k_{Q,Q_0} takes the detector response for the actual beam quality, Q, into account.

At the monochromatic beamline, D is the dose at the PMMA phantom surface ($z = 0$), while, at the white-beam beamline, we consider that the measured dose at a given depth, z, in PMMA will be equal to that at a depth $z' = \rho_{\mathrm{PMMA}} \cdot z$ in water.

Equation (2) partly deviates from the formula recommended in the IAEA TRS-398 code of practice, especially due to the effects of PMMA in the determination of calibration and quality correction factor. In other words, we assume that dose differences due to material properties and consequent differences in secondary-particle distribution are negligible. Moreover, we introduce an output correction factor, $K_{f,Q}$,

which considers the effects of field size differences with respect to those in which the detectors were calibrated. This factor cannot be entirely described by the field output factor recommended by the IAEA TRS-398 code of practice. Also, due to the small beam divergence, we assume that the effect of different geometries (source-to-surface distance, in particular) during calibration and measurement are negligible. We therefore define $K_{f,Q}$ according to the IAEA TRS-483 code of practice (International Atomic Energy Agency 2017), despite the fact that this is only valid for megavoltage x-ray beams. Further details regarding the assessment of k_{Q,Q_0} and $K_{f,Q}$ are given in the supplementary material.

Finally, the dose rate, $\dot{D}$, is calculated from beam height, scan velocity, and absorbed dose (integrated over the vertical profile) (Prezado *et al* 2011):

$$\dot{D} = \frac{v_{\text{scan}} \cdot D}{h_{\text{beam}}}. \tag{3}$$

Since dose rate and beam shapes can slightly change with time, these parameters need to be evaluated at each beam time for choosing the correct irradiation setting.

Moreover, the PETRA III ring current varied between 100 mA and 120 mA for different beam times. From equation (3), it is possible to scale dose rate values for comparisons, as follows:

$$D = \frac{\dot{D} \cdot h_{\text{beam}}}{v_{\text{scan}}} = \frac{I \cdot \dot{D}_{\text{scaled}} \cdot h_{\text{beam}}}{v_{\text{scan}}}, \tag{4}$$

where I is the actual current of the storage ring and $\dot{D}_{\text{scaled}}$ the dose rate scaled by I (Fournier *et al* 2016).

At the monochromatic beamline P21.2, the absorbed dose at the phantom surface can be approximated with the collision kerma, K_c. In fact, we can assume to have CPE at the phantom surface, since the range of 45 keV electrons in PMMA (in the continuous slowing down approximation) is 0.03 mm (Berger *et al* 1999). This also ensures lateral CPE for field sizes in the order of a few millimetres. Therefore, from the definition of collision kerma (Ma *et al* 2001):

$$D \approx K_c = \frac{\mu_{\text{en}}}{\rho} \cdot E \cdot \Phi, \tag{5}$$

where μ_{en}/ρ is the mass energy absorption coefficient of the mono-energetic photons, with energy E and fluence Φ, in the considered material. Equation (5) enables for checking the consistency of the experimental values from equation (2) at the monochromatic beamline P21.2 (see also supplementary material) (Ma *et al* 2001).

As mentioned above, a set of Cu absorbers is used at the white-beam beamline P61A to reduce the beam intensity. This avoids damage to sensitive beamline components (such as cameras and detectors), as well as to the experimental set-up. However, the use of filters does not only decrease the dose rate but also hardens the photon beam, thus modifying the shape of the depth dose curve. We therefore carried out a dosimetric characterisation of the beamline P61A for different copper filter thicknesses.

2.5.1. Application example: irradiation of a mouse phantom

To verify our workflow for *in-vivo* experiments, we simulated a mouse irradiation with the help of an anatomically detailed phantom, shown in figure 6. The mouse phantom is produced by means of additive manufacturing using a stereolithography process (Wegner *et al* 2023). It consists of two parts and is primarily composed of clear resin, which serves as surrogate for mouse soft tissue. Additionally, bones, lungs, and several internal organs are implemented in the phantom (Wegner *et al* 2023).

We first exposed the mouse phantom to a single BB and then simulated the dose delivery to a more realistic target volume, with a width of 10 mm. For this purpose, we used a dose-painting technique. Briefly, we translated the stage horizontally after having irradiated a stripe of the target volume with a single beam. In this way, we laterally 'patched' several beams. Prior to the mouse phantom exposure, we optimised the horizontal step movement of the stage with the help of a visual check of irradiated films, as demonstrated in figure 6. This avoids underdosage, if the horizontal step is too large, or overdosage, if this is too small and the fields overlap. After determining the dose rate as described in section 2.5, we adapted the scan velocity for a beam height of 1 mm to deliver a nominal dose of about 45 Gy to the phantom abdomen and brain, respectively. For verification, we positioned a film in the sagittal plane in the middle of the mouse phantom (see figure 6), at a maximum depth of approximately 10 mm.

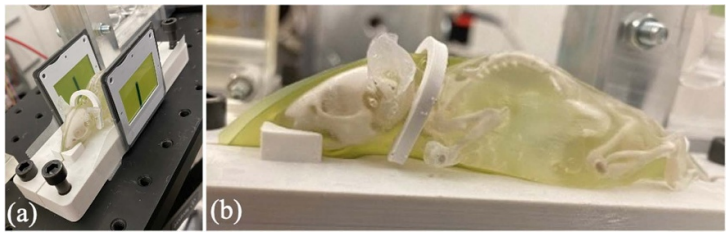

Figure 6. Experimental set-up for irradiations with the mouse phantom, positioned on the experimental stage. The films placed in front and behind the phantom (a) show how we checked the stage horizontal translation for dose-painting through beam patching. For dose verification, a film is placed in the sagittal plane in the middle of the phantom (b).

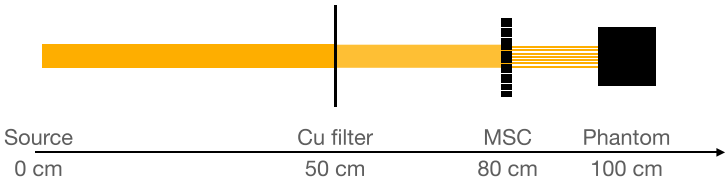

Figure 7. Schematic representation of the MC simulation set-up. The photon source is positioned at $z = 0$, being z the direction of the simulated photons. The Cu filter blocks used at the white-beam beamline P61A are placed at $z = 50$ cm. The MSC and the PMMA phantom centre are at $z = 80$ cm and $z = 100$ cm, respectively.

2.6. Microbeam evaluation

We conducted all microbeam studies placing the X-Tream detector, in edge-on orientation, in the PMMA phantom, without material in front of it. Due to the detector geometry, this still corresponds to a measurement at a PMMA depth of 5 mm. We calculated the PVDR as suggested by Lerch *et al* (2011). According to this method, the PVDR is evaluated independently for each peak. The dose in the valley is averaged over 50 μm, while the peak dose is considered to be the maximum peak value. The PVDR is then determined after calculating the mean values of all PVDRs in the beam area for which the dose profile is flat.

2.7. MC simulations

A MC model of our experimental set-up offers several advantages, since the beamlines at PETRA III are not designed for biomedical experiments. On the one hand, the very small beam size is challenging for absorbed dose measurements with common clinical dosimeters. The comparison between MC calculated and experimental absorbed dose at the monochromatic beamline P21.2 will further prove the consistency of the method and benchmark the simulation model. On the other hand, through simulations of the white-beam beamline P61A, we can verify the suitability of the calculated photon energy spectrum for dosimetry studies. In fact, the shape of the depth dose curve is sensitive to changes in the photon spectral composition. As mentioned in section 2.1.2, due to the very high photon intensity, the x-ray spectral distribution and fluence rate of this beamline could not yet be measured. Finally, the MC simulation allows for a rough estimate of the photon fluence rate at the beamline P61A, as we will show below.

We performed all MC simulations that are relevant for this study with the Geant4 package (version 10.5.1) (Agostinelli *et al* 2003). In our simulation model, the experimental set-up is placed in a 4 m $\times$ 4 m $\times$ 4 m air-filled world. The photon source is positioned 100 cm away from the PMMA phantom centre, with the beam central axis aligned to that of the phantom. The beam size is considered to be rectangular, with dimensions taken from the measured dose profiles. The initial photons are assumed to be homogeneously distributed over the field, thus producing a flat profile in both dimensions. Furthermore, the beam is assumed to be mono-directional (see figure 7). This approximation is acceptable, at least for the simulations without MSC, since the beam divergence is very small. For example, at the beamline P21.2 the divergence for a beam size of 4 mm $\times$ 2 mm (horizontal and vertical) is 27 μrad and 13 μrad, respectively. The simulated PMMA cubic phantom is 10 cm in size, as in the experiments conducted to obtain depth dose curves. For the simulations with microbeams, the MSC is positioned 20 cm upstream with respect to the phantom surface. The MSC is represented by 125 tungsten blocks, with a centre-to-centre spacing of 0.4 mm and each having the following dimensions: 8 mm thickness, 3 mm height and 0.35 mm width.

The Cu filtering blocks at the white-beam beamline P61A, included in the simulation set-up, are positioned 50 cm away from the phantom (centre-to-centre spacing).

We calculated the absorbed dose in the phantom using different scoring meshes, the sizes of which are adapted depending on the goal of the simulation. For the evaluation of the beam dose profile with and without the MSC, the chosen spatial resolution is 0.01 mm × 0.2 mm × 0.5 mm, while this is 0.2 mm × 0.2 mm × 1.0 mm for the depth dose curves. The dose rate from the simulation is related to the absorbed dose, D_{MC}, as follows:

$$\dot{D}_{MC} = \frac{\Phi}{N_{sim}} \cdot D_{MC}. \tag{6}$$

Here, N_{sim} is the number of simulated photons per unit area and Φ the photon fluence rate at the beamline, in $s^{-1} \cdot cm^{-2}$.

We carried out the MC simulations of the monochromatic beamline P21.2 for primary photon energies of 45 keV and 60 keV. The calculation of the absolute dose rate from the simulation results (equation (6)) requires the photon fluence rate to be known precisely. We measured the photon fluence rate at this beamline during each experiment, with a calibrated photodiode. This data is therefore important to verify the consistency between measurements and simulations and provides a good indicator of the validity of our method.

For the white-beam beamline P61A, the initial photon spectrum implemented in the MC simulation is the one shown in figure 1. Due to the very high photon fluence rate (estimated to be about $4 \cdot 10^{16}$ photons $(s \cdot cm^2)^{-1}$), we could not yet measure the photon spectrum at the phantom surface. Using equation (6), we can, however, assess the photon fluence from the simulation, provided that the absorbed dose is measured correctly.

3. Results

In the following, we first present the results obtained at the monochromatic beamline P21.2. This data represents a benchmark for the procedure followed in this study, which was then adapted for the conditions at the white-beam beamline P61A.

We determined the uncertainties according to the recommendations of the ISO *Guide to the expression of uncertainty in measurement* (Joint Committee for Guides in Metrology 2004). Details can be found in the supplementary material.

3.1. Monochromatic beamline (P21.2)

3.1.1. Dose profiles

We report the relative horizontal dose profile with flat top at the beamline P21.2 in figure 8(a). This was measured both with the X-Tream system and the MD. Both datasets show a comparable structure, with relative deviations below ±5%. The FWHM is 3.2 mm when measured with the X-Tream system and 3.3 mm with the MD, respectively. The flat-top vertical profile, shown in figure 8(b), has a FWHM of 1.6 mm.

3.1.2. Depth dose curves

Figure 9(a) illustrates the relative depth dose curves in PMMA obtained with MD, films, and X-Tream system, respectively, for an x-ray energy of 45 keV and a photon field size of (3.3 × 1.6) mm^2. For depths between 5 and 12 mm, the agreement between film, MD, and X-Tream system is very good. Starting at a depth of 15 mm, the MD measures a higher relative dose compared to the X-Tream, with a maximum discrepancy of 9% at larger depths.

A comparison between the depth dose curve acquired with the X-Tream system and the simulated one (figure 9(a)) shows an excellent agreement. This is the most accurate comparison, since both the MC simulation and the measurements with the X-Tream detector were performed without vertical translation of the phantom through the beam.

In a second experiment, we also measured depth dose curves for an energy of 60 keV with MD and films (see figure 9(b)). The experimental data from the MD and the MC simulation results are in good agreement, with a maximum relative discrepancy of about ±4%. The film data deviates in the first millimetres from simulation and MD data, while the MD data is slightly larger than the simulated one at depths larger than 15 mm.

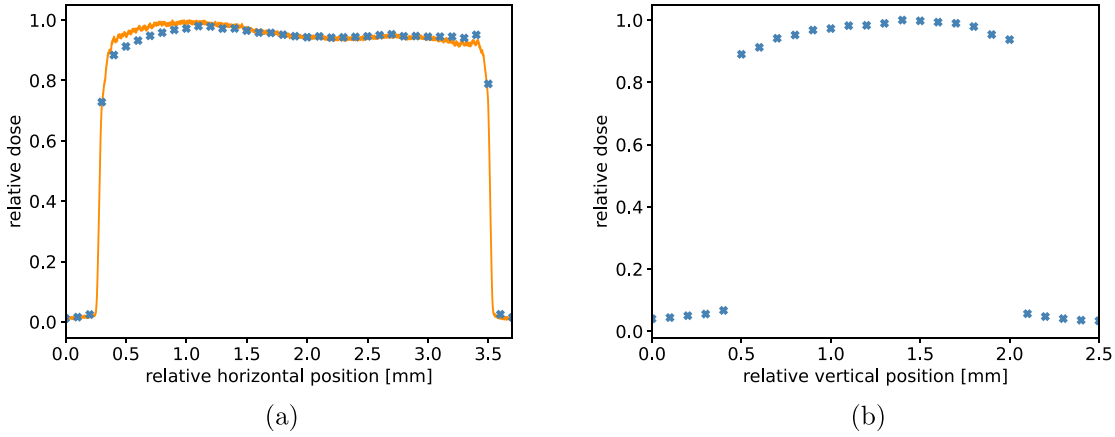

Figure 8. Relative horizontal (a) and vertical (b) dose profile at the beamline P21.2, normalised at the field maximum. The horizontal profile is measured with the MD (blue) and X-Tream system (orange) while the vertical profile is measured with the MD, only. Both dosimeters are positioned in edge-on orientation with respect to the beam direction, as shown in figure 3. The X-Tream detector is moved with a constant velocity of 10 mm s^{-1} through the beam. The scan velocity is used to convert the time resolution of the system to a relative horizontal position in the beam. Measurements with the MD are performed without PMMA in front and in a static way, with the motor moving in 0.1 mm steps. The X-Tream data is recorded in 5 mm PMMA depth.

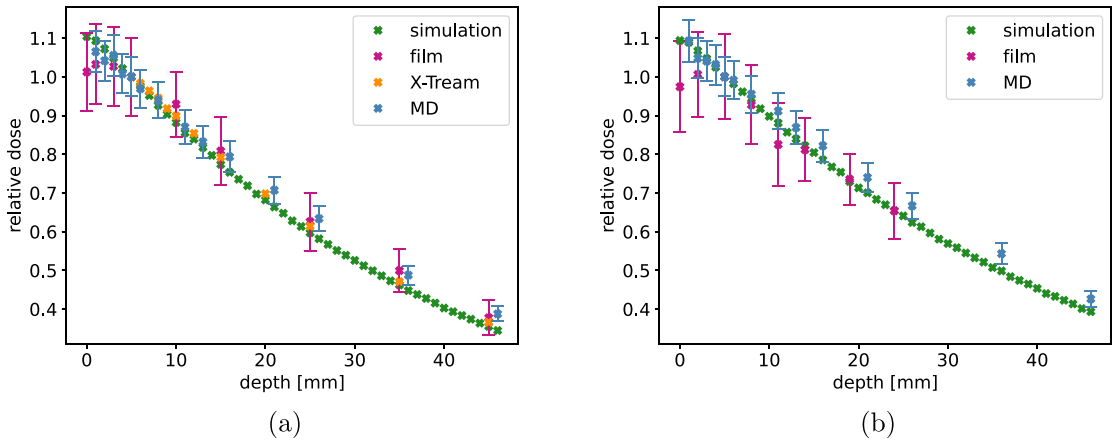

Figure 9. Relative depth dose curves at the beamline P21.2 for a photon energy of 45 (a) and 60 keV (b) and a field size of 3.3 mm × 1.6 mm. These curves are measured in the PMMA plate phantom (10 cm in size) with the MD and films and also with the X-Tream system for 45 keV photon energy (a). The MC simulated data is shown as well. The X-Tream detector is positioned in edge-on orientation and kept stationary. The film and MD measurements are performed by moving vertically through the beam, with a constant velocity of 1.6 mm s^{-1} (1.0 mm s^{-1}) for 45 keV (60 KeV). For comparison, all results are relative to the dose value at 5 mm depth. The simulation was carried out for 10^{10} starting photons and the relative standard deviation of the results is up to ±1.4% at larger depths. The error bars represent the overall uncertainty with a coverage factor $k = 2$. A comprehensive uncertainty analysis is provided in the supplementary material. For both simulated and X-Tream data, the symbols are larger than the error bars.

3.1.3. Absolute dose

Table 1 reports the experimental dose rate from dynamic measurements (equation (3)), both using the IC and the MD. This data is compared to the collision kerma rate (equation (5)) and the MC calculated value (from equation (6)). The maximum relative discrepancy of about 25% is between IC measurement and collision kerma approximation and can be considered acceptable for proving data consistency.

3.1.4. Microbeams

Since the dose profile is not perfectly flat, the MB are slightly uneven, as visible in figure 10(a), which also shows that a maximum number of eight MB can be produced at the monochromatic beamline P21.2.

An evaluation of the four peaks in the field centre leads to an average PVDR of 120.5 ± 10.9. We assume that the uncertainty of the PVDR is established by the valley dose uncertainty, estimated from the standard deviation of the valley dose values ($k = 2$), since this measurement depends largely from the low-dose sensitivity of the used detector. However, as the peak dose itself also has an uncertainty (even if much smaller compared to the valley dose), the given uncertainty is a minimum uncertainty.

Table 1. Absolute dose rate assessment at the beamline P21.2 for an x-ray energy of 45 keV, obtained from measurements with both the MD and IC at the PMMA phantom surface. The scanning velocity was 1 mm s^{-1} and the field size 3.3 mm × 1.6 mm. The MD and IC data was corrected for energy and field size dependence according to the results shown in the supplementary material. The measured fluence rate during these experiments was $(1.16 \pm 0.02) \cdot 10^{14}$ s^{-1} cm^{-2}. The overall uncertainty is reported with a coverage factor $k = 2$.

Method	$\dot{D}$ in Gy s^{-1}
IC	26 ± 2
MD	25 ± 2
Equation (5)	32.9 ± 0.3
MC	29 ± 1

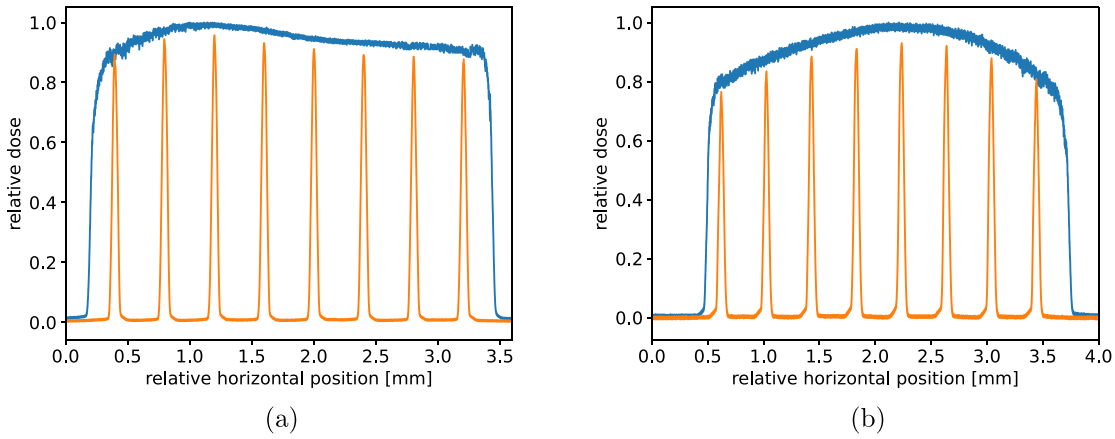

Figure 10. Relative dose profile in the broad beam (blue) and microbeams (orange) at the beamline P21.2 for 45 keV (a) and 60 keV (b), measured with the X-Tream detector in edge-on orientation, moving with a constant velocity of 1 mm s^{-1} horizontally through the beam. The scan velocity is used to convert the time resolution of the system to a relative horizontal position in the beam. All data, taken at a PMMA depth of 5 mm, are relative to the dose maximum of the broad beam.

Since the beam has a small divergence, some photons entering the MSC between the tungsten blocks can still be absorbed in the blocks themselves. Moreover, despite the small range in PMMA of 45 keV electrons, the condition of CPE might not hold in the microbeams. Hence, as expected, the dose in the MB is lower than in the BB. We calculated the dose rate loss due to the MSC by considering the profile height in the beam centre and the height of the fourth MB peak. This loss is about 5%. The simulated PVDR, calculated for the five central peaks, has a mean value of 148.9 ± 8.8, which is about 24% larger than the experimental value. As done for the experiment, we compared the dose rate difference in the peaks to that in the BB. The average difference of all simulated peaks from the BB results to be about 5% and, therefore, in excellent agreement with the experimental value.

Figure 11 gives a closer look at one MB from MC simulation and experiment at 45 keV. Both peak heights are normalised to unity to compare the shape. The structure and FWHM of the MB is very similar for simulation and experiment, with an experimental FWHM of 48 μm and a simulated one of 50 μm, respectively.

We also investigated the beam profile and MB for 60 keV photons. Switching to a different energy yields a slightly different beam profile, in this case reducing the dose flatness. If the beam defining slits are maintained in the same position as for 45 keV, the dose rate variation, between maximum and minimum, is, in fact, about 20%. The peak height of the MBs follows, again, the beam structure and the dose rate loss due to the MSC is about 7% (figure 10(b)).

3.2. White-beam beamline (P61A)

3.2.1. Beam profile

The horizontal profile at the white-beam beamline P61A, measured with X-Tream system and MD, has a sharp left edge but a less sharp dose gradient on the right side, as can be seen in figure 12(a). Additionally, the profile presents a small dose increase towards the right edge, which could be measured with both detectors and presents the same shape and position during different beam times. The measured FWHM is 2.0 mm and the relative deviation between maximum and minimum top dose is less than ±4%.

Figure 12(b) shows two vertical dose profiles, recorded with two different openings of the vertical beam-defining slits. While the dose penumbra is less sharp with respect to that of the horizontal profile,

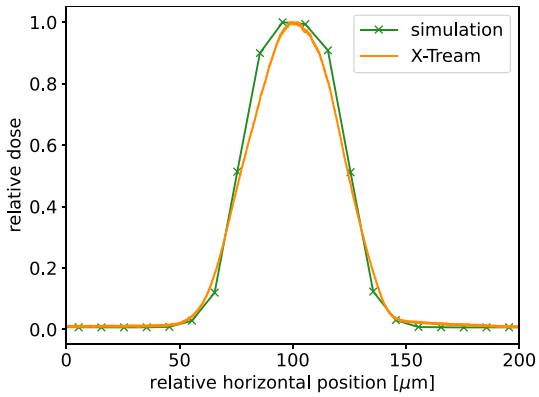

Figure 11. Shape of a microbeam, from simulated (green) and experimental data (orange), at the beamline P21.2 for 45 keV. The X-Tream is moved horizontally through the beam with a constant velocity of 1 mm s^{-1}.

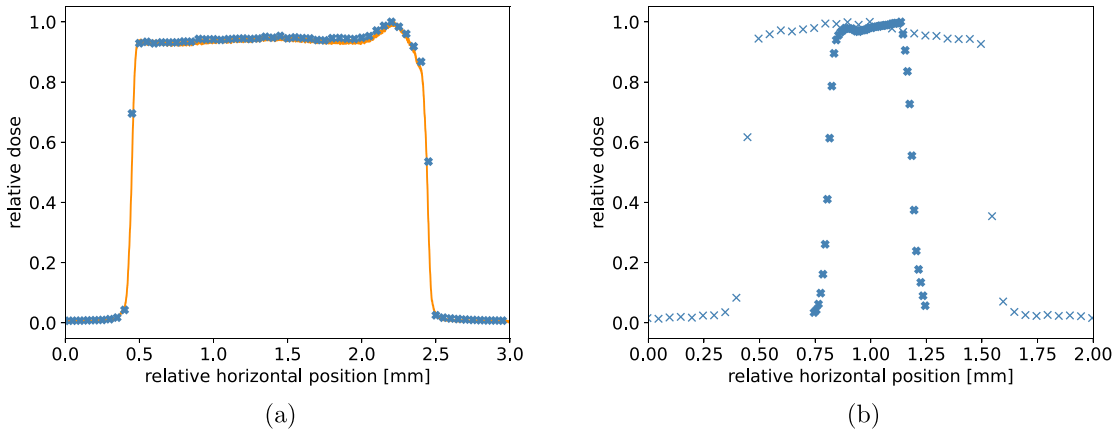

Figure 12. Beam profiles at the beamline P61A. The horizontal profile (a) is measured with X-Tream (orange) and MD (blue), while the two vertical profiles (b), for two different vertical openings, are measured with the MD, only. Both dosimeters are positioned in edge-on orientation and the X-Tream is moved with a constant velocity of 2.5 mm s^{-1} through the beam. The scan velocity is used to convert the time resolution of the system to a relative horizontal position in the beam. For the static measurement with the MD, the motor is moved with 0.1 mm steps horizontally and, respectively, 0.01 mm and 0.05 mm vertically. The profiles are measured at a PMMA depth of 5 mm. All data is relative to the dose maximum.

the top dose value is constant within a few percent. For these two slit openings, the FWHM of the vertical profile is 0.38 mm and 1.1 mm, respectively.

3.2.2. Cu filtering—dose rate reduction and beam hardening

In the following, we summarise the effects of copper filtering on the white-beam. The mentioned material thickness is to be understood as additional filters to the absorbers that are always in place at this beamline. The lowest additional copper filter for this measurement is 1 mm, as less filtration leads to an excessive heat load on the beamline components.

The experimental results of dose reduction for increasing Cu thickness are shown in figure 13, together with the results of the MC simulations. We assessed the statistical uncertainty of the MC simulation by Gaussian propagation of the relative standard deviation for each run. For increasing copper thickness, the statistical uncertainty increases, as we started the same number of events for each filter. While the uncertainty for thicknesses up to 25 mm is below ±2%, this increases to about ±8% for 40 mm Cu. According to the simulation, 1 mm of additional copper reduces the dose rate to 23% of the expected value without additional copper. The comparison between the relative dose rate from simulation and experiments up to a Cu thickness of 27.5 mm is illustrated in figure 13, with a satisfactory agreement (within ±3% and ±10% when comparing with X-Tream and film measurements, respectively).

Figure 14(a) shows, exemplarily, x-ray spectra for 0.5 to 15 mm of Cu absorber thickness, resulting from MC simulations to study the beam-hardening effect of copper filters. The mean energy of

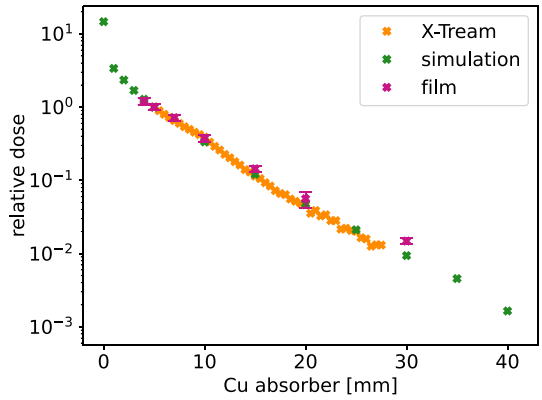

Figure 13. Simulated and measured dose rate relative to the 5 mm Cu filtered dose rate, for thicknesses between 5 and 27.5 mm for the measured dose rates. The X-Tream detector is irradiated in a static way with a field size of 2.4 mm × 1.25 mm, while the films are moved vertically with a velocity of 30 mm s^{-1} through the beam (beam height: 0.88 mm). The MC simulation is started with 10^{10} photons for each copper filter and considers a stationary detector. The error bars represent the overall uncertainty with a coverage factor $k = 2$. The error bars of the X-Tream measurements, as well as of the simulated data, is smaller than the symbols.

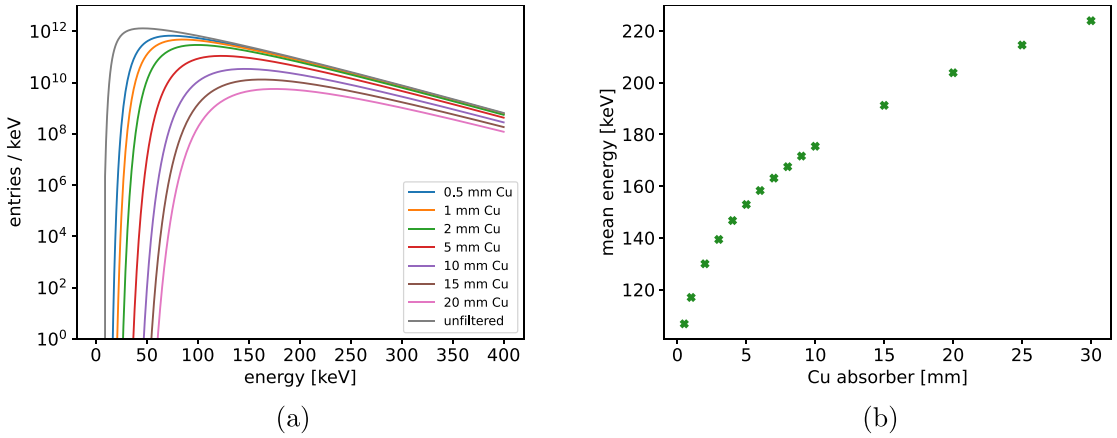

Figure 14. Simulated energy spectra (a) and corresponding mean energy (b) for increasing copper absorber thickness. A total of 10^{10} photons are simulated for each copper filter. The photon energy distribution was scored at the phantom position and the mean energy was calculated using equation (1).

the photon beam with 1 mm Cu is 117 keV, compared to 83 keV with no Cu absorber, and increases to about 220 keV for a thickness of 30 mm (figure 14(b)).

3.2.3. Depth dose curves

We observed a general satisfactory agreement between different data for relative depth dose curves. Examples for Cu filters of 2 mm and 10 mm can be seen in figure 15. In particular, the X-Tream results show a lower percentage depth dose than the MC simulation. This is more pronounced for 10 mm Cu, with a maximum discrepancy of 6% at a depth of 40 mm.

The film results are in good agreement with the simulation (within ±10% for all depths in PMMA), but also lower than the simulated data for larger depths. Figure 16 summarises, furthermore, simulated depth dose curves up to a depth of 100 mm for several Cu thicknesses. A substantial change in these curves can be seen for 1 mm compared to 0 mm additional Cu. In fact, the relative dose decreases to 50% of the surface dose at a depth of 13 mm without filter, while this reduction takes place at a depth of 38 mm for 1 mm Cu. For larger copper thicknesses, the changes in the depth dose curve are less pronounced. With 10 mm Cu, a dose reduction of 50% is reached at a depth of 42 mm in PMMA.

3.2.4. Absolute dose measurements

Table 2 reports the results of dynamic absorbed dose measurements with MD and films at two different scanning velocities for several filter thicknesses. The maximum discrepancy between the two sets of corresponding dose rate values (see equation (3)) is below ±7%, except for the highest dose rate, where the MD value is larger than the film value by about 9%.

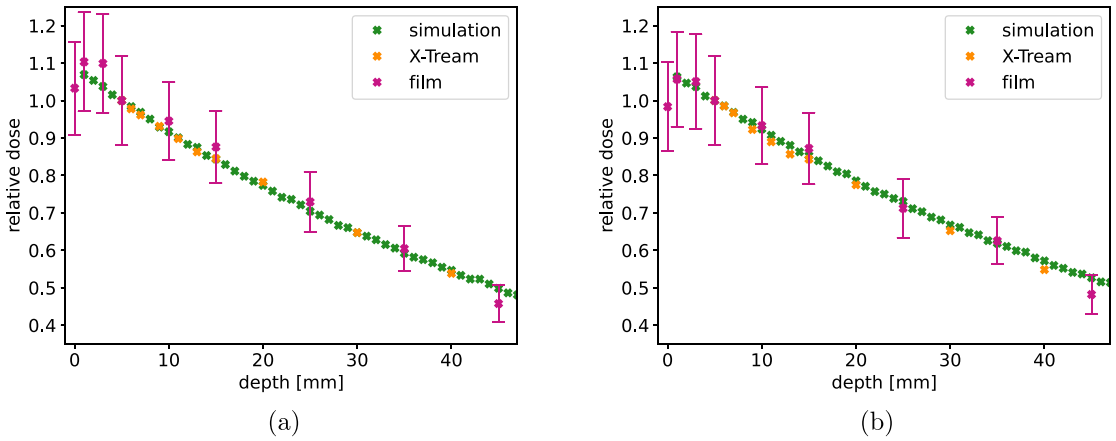

Figure 15. Comparison between experimental and simulated relative depth dose curves at the beamline P61A with an additional Cu filter of 2 mm (a) and 10 mm (b). Field size: 1.8 mm × 0.7 mm. The dose is normalised to a depth of 5 mm. The X-Tream measurements are performed statically, while the films are scanned through the beam with a constant velocity of 30 mm s^{-1}.

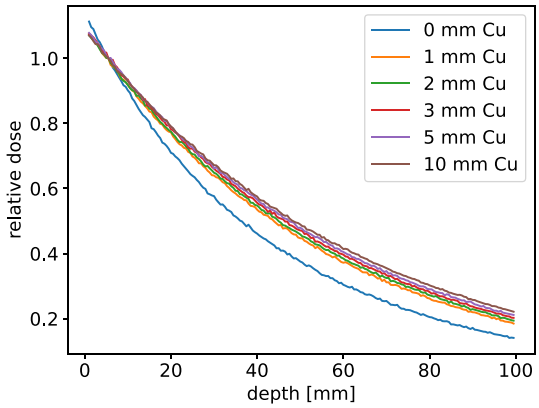

Figure 16. Simulated depth dose curves for 0 to 10 mm of Cu at the beamline P61A. For each copper absorber, 10^{10} photons are simulated, increasing the uncertainty with thicker copper absorber. For 5 mm of copper absorber thickness, the overall uncertainty of the MC calculation is less than ±5%, while the uncertainty is below ±2% with 0 mm of copper absorber. The results are relative to the value at 5 mm depth in PMMA.

Table 2. Absolute dose rate assessment at the white-beam beamline P61A for different Cu thicknesses, obtained from dynamic absolute dose measurements with both the MD in edge-on orientation and films. For each Cu thickness, we report the mean energy of the simulated x-ray spectrum, E_{mean}. The MD data is corrected for energy and field size dependence according to the results shown in the supplementary material. The beam width is 1.8 mm. All measurements are performed in the PMMA phantom at a depth of 5 mm for $h_{beam} = 0.77$ mm.

Cu thickness in mm	E_{mean} in keV	Dosimeter	v_{scan} in mm s^{-1}	D in Gy	$\dot{D}$ in Gy s^{-1}
7	163	MD	0.77	1908 ± 133	1908 ± 133
		Film	10.55	127 ± 13	1747 ± 175
10	175	MD	0.77	961 ± 67	961 ± 67
		Film	5.34	141 ± 14	979 ± 98
15	191	MD	0.77	375 ± 26	375 ± 26
		Film	2.08	136 ± 14	366 ± 37
19	201	MD	0.77	192 ± 13	192 ± 13
		Film	0.558	263 ± 26	191 ± 19
25	214	MD	0.77	79 ± 6	79 ± 6
		Film	0.44	130 ± 13	74 ± 7
30	224	MD	0.77	38 ± 3	38 ± 3
		Film	0.21	141 ± 14	38 ± 4

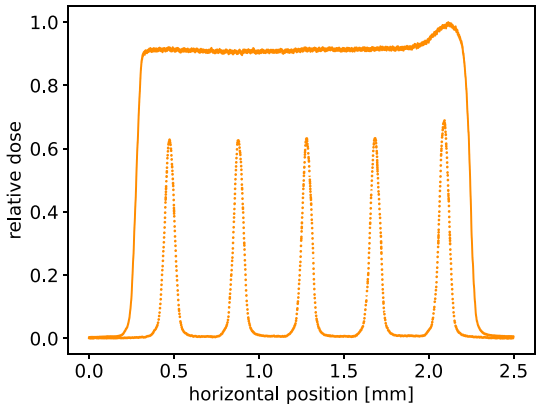

Figure 17. Microbeams (dotted line) at the beamline P61A measured with the X-Tream in edge-on orientation, compared with the broad beam profile (solid line). 10 mm PMMA was placed in front of the detector and the additional filter was 10 mm Cu. The horizontal velocity was 1.0 mm s^{-1}. The scan velocity was used to convert the time resolution of the X-Tream dosimetry system to a relative horizontal position in the beam.

Using equation (6) and the relative dose rate from figure 16, we estimate a photon fluence rate of $3.2 \cdot 10^{16}$ photons $(s{\cdot}cm^2)^{-1}$, which is close to the expected value of about $4 \cdot 10^{16}$ photons $(s{\cdot}cm^2)^{-1}$.

3.2.5. Microbeams

We used the X-Tream system in edge-on orientation to measure PVDR and dose rate reduction due to the MSC at the beamline P61A in a similar way as at the beamline P21.2 (see figure 17). Due to the shape of the beam profile, the fifth peak on the far right side is about 9% higher than the other four peaks. Among these, the difference in peak height lies below 2%, following the shape of the beam. Figure 17 also shows a non-symmetrical structure of the MBs, with a slower dose increase on the left side compared to that on the right side, which is due to the detector geometry. For these reasons, we considered the three peaks in the centre of the field to determine both PVDR and difference in dose rate between BB and MB. The average PVDR of these three peaks with a Cu filtration of 10 mm in a depth of 10 mm in PMMA results to be 100 ± 8.5, while the average dose rate difference from MB to BB is about 30%.

The MC simulation with the MSC in place and an additional Cu thickness of 10 mm results in an average PVDR of 121.5 ± 4.5, which is considerably larger than the experimental value. Nevertheless, the experimental FWHM of the central MB of 56.5 μm is in good agreement with the simulated value of 50 μm. Unfortunately, the agreement is less good for the dose rate reduction due to the MSC with a simulated value (5.5%), much lower than that evaluated from experiments.

The simulated PVDR, calculated as a function of depth in PMMA without additional Cu, can also be seen in figure 18, together with the results obtained for the beamline P21.2. Both at the monochromatic and at the white-beam beamline, the PVDR value is energy dependent, decreases drastically up to a depth of 5 mm in PMMA and remains almost constant for larger depths. At the P21.2 beamline, the PVDR at 45 keV is smaller than at 60 keV, while the opposite can be observed at the P61A beamline, where the PVDR decreases for increasing mean x-ray energy.

3.2.6. Mouse phantom irradiations

To verify our irradiation protocols for future pre-clinical experiments, we considered two types of hypothetical targets in the mouse abdomen: (i) as large as the beam (about 2 mm in width) and (ii) 10 mm in width, which was covered using a dose-painting technique. This was implemented by laterally patching five beams with a stage step translation of 2 mm. We carried out these experiments with a Cu filter of 19 mm thickness. The corresponding dose rate during this experiment, measured at 5 mm PMMA depth, was (223 ± 22) Gy s^{-1}. For a scan length of 1.1 mm, we chose a scan velocity of 4.4 mm s^{-1} to deliver 50 Gy at 5 mm depth. Considering the shape of the depth dose curves, also for the phantom material (see supplementary material), we expect a maximum dose reduction of about 10% at the maximum depth of 10 mm, thus resulting in a nominal dose of 45 Gy in the abdominal region. An example of measured dose profiles, presented in figure 19, demonstrates a satisfactory agreement between expected and delivered dose. In fact, the mean dose value in the target volume for the shown irradiations is (43 ± 6) Gy. For the extended target width of 10 mm, over- or under-dosage due to beam patching is below $\pm 15\%$.

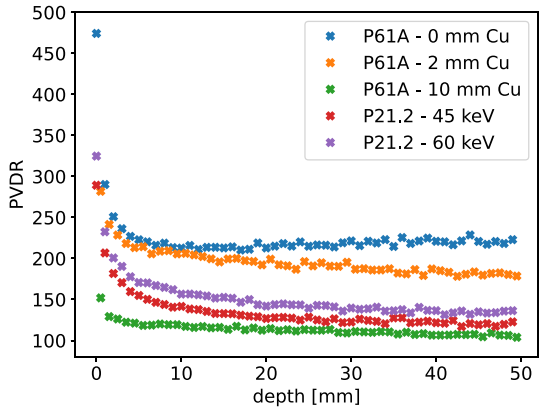

Figure 18. MC simulation of the PVDR as a function of depth in PMMA for 45 and 60 keV (P21.2) and for the white-beam without additional Cu absorber and for 2 and 10 mm of Cu (P61A). The PVDR is calculated as the mean value from the five (P21.2) and four (P61A) peaks in the centre of the profile for left and right valley, respectively.

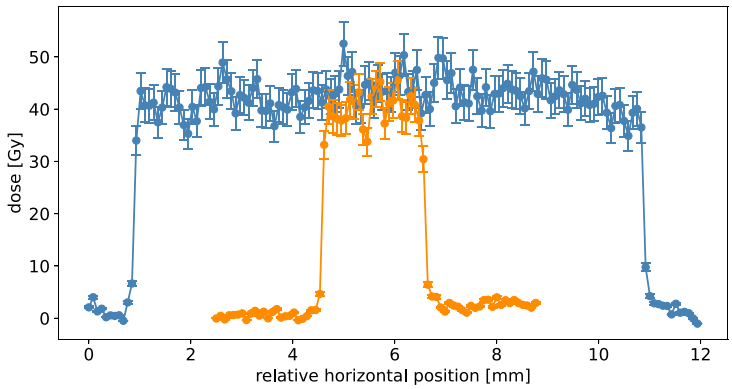

Figure 19. Dose profiles for a single beam (orange) and dose painting with five patched beams (blue), measured in the abdominal region of the mouse phantom, with films placed in the sagittal plane that cuts the phantom along the midline. The nominal dose was 45 Gy. The error bars represent the total uncertainty of the measured ratio, with a coverage factor $k = 2$.

4. Discussion and conclusions

This work shows potential and challenges of performing SFRT and UHDR radiotherapy research studies at synchrotron beams characterised by very small beam sizes, such as those of the PETRA III synchrotron at DESY (Hamburg). With a thorough investigation of the dosimetric properties of the white-beam beamline, which we conducted for the first time, we offer users the possibility of carrying out systematic pre-clinical studies on the effects of UHDR over a wide range of dose rates.

Due to the small beam size, we assessed correction factors for the detectors used in this study, which were calibrated by the manufacturer in cm-sized fields, where the condition of lateral CPE are satisfied for photon energies used in clinical radiotherapy (up to a few MeV). With the assessment of specific correction factors, we can compensate for dose-volume effects, lack of CPE, and, if necessary, for energy dependence. The resulting correction factors for the MD, both for field size and energy dependence, are in the same order of magnitude as those found in other studies (Livingstone *et al* 2016, Brace *et al* 2020, Kaveckyte *et al* 2020). This confirms, once more, the importance of thoroughly characterising radiation detectors if working with radiation fields that are different from those used for calibration.

The second challenge that we face at the white-beam beamline is the very-high photon fluence rate. This hindered, up to now, the direct measurement of the beam spectrum and its intensity. For this reason, the investigation of the monochromatic beamline provided a benchmark for the procedure adopted in this work, since the photon fluence rate can be precisely measured at this beamline. A precise knowledge of the photon fluence rate allowed us to verify the accuracy of the experimental dose rate by comparing this data to the theoretical value in the kerma approximation. Moreover, the good agreement between the experimental dose rate obtained with the calibrated IC and the MD provides a solid base for studies at the white-beam beamline.

The procedure developed in this study enables one to measure the dose rate with a relative overall uncertainty in the order of ±10%, both at the monochromatic and at the white-beam beamline. While the dose rate at the monochromatic beamline P21.2 is approximately 30 Gy s^{-1}, we can vary it reliably between about 20 Gy s^{-1} and 1.8 kGy s^{-1} at the white-beam beamline, thus enabling systematic studies of the biological effect of UHDRs in the future.

As part of the dosimetric characterisation, we observed, as to be expected, an energy-dependent dose deposition in depth. However, the changes in the depth-dose curve at the white-beam beamline are negligible for Cu thicknesses larger than 1 mm, so that beam-quality effects should not play any significant role in UHDR experiments conducted at this beamline at different dose rates.

When inserting the MSC, the average dose rate drop in the MB with respect to the BB at the beamline P61A is about 30%, much larger than the loss at the beamline P21.2 (approximately 5%). The explanation most likely lies in the wiggler source of the white-beam beamline causing a larger divergence than found at the monochromatic beamline. A larger divergence leads to a larger dose rate loss in the MSC, because the collimator will absorb converging photons, while these would contribute to the energy deposited by the BB. Moreover, due to the higher x-ray energy at the white-beam beamline, the range of the most energetic secondary electrons in PMMA is larger than 1 mm, thus causing a general violation of the lateral CPE. The lack of lateral CPE is more pronounced in the MB.

During this study, we also demonstrated that it would be possible to irradiate small animals at PETRA III by applying a dose-painting technique. Despite the fact that neither image guidance for positioning, nor an image-based treatment planning system were available, the maximum discrepancy between prescribed and delivered dose in a 10 mm wide target volume in the abdominal region of the mouse phantom was about ±15%. Considering further contributions to the total experimental uncertainty, such as the shape of the depth dose curve and the fact that the phantom is not homogeneous, we evaluate this first application as successful.

Furthermore, we performed MC simulations with a simple representation of beamline and set-up, taking only the main components into account. Nevertheless, at both beamlines, the agreement between simulated depth dose curves for BB irradiations and those measured with the X-Tream dosimetry system in stationary mode is very good. Also, the MC simulation results in terms of absolute dose rate of the beamline P21.2 are in line with the experimental data, therefore confirming that this simple representation is acceptable and accurate for dosimetry. The general consistency between experiments and MC simulation of the BB for both beamlines is an indicator of the fact that other approximations, such as using a mono-directional beam with a rectangular shape and homogeneous intensity, are acceptable. Moreover, we can state that the initial photon spectrum used for the simulations of the P61A well represents the actual spectrum for dose calculations.

MC simulation results including the MSC show that the structure of the simulated depth-dependence of the PVDR is similar at both beamlines and in line with experimental and simulated data from other groups (Bartzsch *et al* 2015). Hence, for irradiations at a depth of 5 mm or larger, we can assume an almost constant PVDR, within the overall calculation uncertainties. Interestingly, at the P21.2 beamline, the PVDR increases with increasing energy, while the opposite is observed at the P61A beamline. Since the valley dose is strongly affected by primary and secondary scattering events, it is important to perform experiments for comparison.

This study has several limitations, which we will briefly discuss in the following. First, we did not yet entirely follow an internationally-recognised clinical dosimetry protocol, such as the IAEA Technical Report No. 398 (International Atomic Energy Agency 2024) or the AAPM Technical report of the Task Group 61 (Ma *et al* 2001), which, especially for beam qualities at the beamline P61A, recommends to perform absolute dosimetry in a water-equivalent phantom at a depth of 20 mm, while we measured the absorbed dose at a depth of 5 mm in PMMA. Also, in the future, the MD should be calibrated for the actual conditions at the beamline, i.e. at lower photon energies in addition to ^{60}Co, as well as for exposures in edge-on orientation. This would further reduce the total experimental uncertainty and allow us to identify potential errors and systematic deviations.

To be in line with international protocols, it will also be necessary to verify that the procedure to determine the output correction factor, recommended in the IAEA Technical Report No. 483 (International Atomic Energy Agency 2017), is valid for low-energy photons. In other words, we will carry out studies to determine whether the output correction factor for radiochromic films is unity for dose measurements in low-energy spectra. While this can be considered as a good approximation for spectra comparable to that of the white-beam beamline, this should be accurately verified for the dosimetry at the monochromatic beamline. However, the comparison of different approaches, as conducted in this study, confirms that the definition is valid within the current experimental uncertainties.

Finally, the MC simulation model of the beamlines needs to be refined for a better performance in the presence of the MSC. In fact, the measured PVDR is lower than the simulated one. Beamline components not included in the simulation could cause more photon and secondary-electron scattering and, therefore, increase the valley dose, with a lower experimental PVDR as a result. Additionally, the beam divergence and the actual beam dose profile can lead to discrepancies in the PVDR between simulation and experiment. Even if the beam divergence is small, it has an effect on the scattering properties of the photons and can increase the valley dose. However, since full MC simulations of the beamlines require large human and computational resources, in the future we will first implement the actual beam shape and divergence, which are fundamental for MRT dose calculations.

In conclusion, we were able to demonstrate that with the robust dosimetric procedure adopted in this work, biomedical researchers will have the opportunity to conduct radiotherapy studies at beamlines of the PETRA III synchrotron at DESY. At the same time, this procedure can be easily adopted at different synchrotron centres, should further millimetre-sized beamlines become available for radiotherapy research in the future.

Data availability statement

All data that support the findings of this study are included within the article (and any supplementary information files).

Acknowledgments

We acknowledge DESY (Hamburg, Germany), a member of the Helmholtz Association HGF, for the provision of experimental facilities. Parts of this research were carried out at PETRA III. Beamtime was allocated for Proposals I-20211383, I-20211485, and I-20230467. E G and M W also would like to acknowledge the 'Forschungszentrum Medizintechnik' (FMTHH, Hamburg) and the Hamburg 'Behörde für Wissenschaft, Forschung und Gleichstellung' (BWFG) for funding parts of this research (PEEK project and graduate school 'Innovative Technologies in Cancer Diagnostics and Therapy', respectively).

ORCID iDs

Catharina Mewes 0009-0000-8201-8666
Michael Lerch 0000-0002-2406-9972
Marco Petasecca 0000-0001-5958-7457
Ulrich Lienert 0000-0002-8842-5657
Elisabeth Schültke 0000-0002-1273-0065
Jason Paino 0000-0002-3648-7880
James Cayley 0009-0006-9037-770X
Marie Wegner 0000-0001-8616-859X
Stefan Fiedler 0000-0002-3623-3311
Elisabetta Gargioni 0000-0002-8204-0609

References

Adam J-F *et al* 2022 Toward neuro-oncologic clinical trials of high-dose-rate synchrotron microbeam radiation therapy: first treatment of a spontaneous canine brain tumor *Int. J. Radiat. Oncol. Biol. Phys.* **113** 967–73

Agostinelli S *et al* 2003 Geant4—a simulation toolkit *Nucl. Instrum. Methods Phys. Res. A* **506** 250–303

Al-Zeer M A, Prehn F, Fiedler S, Lienert U, Krisch M, Berg J, Kurreck J, Hildebrandt G and Schültke E 2022 Evaluating the suitability of 3D bioprinted samples for experimental radiotherapy: a pilot study *Int. J. Mol. Sci.* **23** 9951

ANSTO 2025 Beamtime guide—imaging and medical (available at: www.ansto.gov.au/research/user-office/instruments/beamlines/imaging-and-medical/beamtime-guide) (Accessed May 2025)

Ashland 2025 Gafchromic HD-V2 film specifiction and user guide (available at: www.gafchromic.com/gafchromic-film/radiotherapy-films/HD-V2/index.asp) (Accessed May 2025)

Bartzsch S, Lott J, Welsch K, Bräuer-Krisch E and Oelfke U 2015 Micrometer-resolved film dosimetry using a microscope in microbeam radiation therapy *Med. Phys.* **42** 4069–79

Berger M, Coursey J and Zucker M 1999 ESTAR, PSTAR, and ASTAR: computer programs for calculating stopping-power and range tables for electrons, protons, and helium ions (version 1.21) (available at: http://physics.nist.gov/Star) (Accessed May 2025)

Bourhis J *et al* 2019a Clinical translation of FLASH radiotherapy: why and how? *Radiother. Oncol.* **139** 11–17

Bourhis J *et al* 2019b Treatment of a first patient with FLASH radiotherapy *Radiother. Oncol.* **139** 18–22

Brace O J, Alhujaili S F, Paino J R, Butler D J, Wilkinson D, Oborn B M, Rosenfeld A B, Lerch M L F, Petasecca M and Davis J A 2020 Evaluation of the PTW microdiamond in edge-on orientation for dosimetry in small fields *J. Appl. Clin. Med. Phys.* **21** 278–88

Bräuer-Krisch E, Requardt H, Brochard T, Berruyer G, Renier M, Laissue J A and Bravin A 2009 New technology enables high precision multislit collimators for microbeam radiation therapy *Rev. Sci. Instrum.* **80** 074301

Bräuer-Krisch E, Serduc R, Siegbahn E A, Duc G L, Prezado Y, Bravin A, Blattmann H and Laissue J A 2010 Effects of pulsed, spatially fractionated, microscopic synchrotron x-ray beams on normal and tumoral brain tissue *Mutat. Res./Rev. Mutat. Res.* **704** 160–6
Chen S N *et al* 2016 Absolute dosimetric characterization of Gafchromic EBT3 and HDV2 films using commercial flat-bed scanners and evaluation of the scanner response function variability *Rev. Sci. Instrum.* **87** 073301
Crosbie J C *et al* 2010 Tumor cell response to synchrotron microbeam radiation therapy differs markedly from cells in normal tissues *Int. J. Radiat. Oncol. Biol. Phys.* **77** 886–94
Davis J A *et al* 2021 X-TREAM protocol for in vitro microbeam radiation therapy at the australian synchrotron *J. Appl. Phys.* **129** 244902
Davis J A, Paino J R, Dipuglia A, Cameron M, Siegele R, Pastuovic Z, Petasecca M, Perevertaylo V L, Rosenfeld A B and Lerch M L F 2018 Characterisation and evaluation of a PNP strip detector for synchrotron microbeam radiation therapy *Biomed. Phys. Eng. Express* **4** 044002
Devic S, Tomic N, Soares C G and Podgorsak E B 2009 Optimizing the dynamic range extension of a radiochromic film dosimetry system *Med. Phys.* **36** 429–37
ESRF 2025 *ID17 - BIOMEDICAL BEAMLINE* (available at: www.esrf.fr/UsersAndScience/Experiments/CBS/ID17) (Accessed May 2025)
Farla R 2022 Extreme conditions research using the large-volume press at the P61B end station, PETRA III *J. Synchrotron Radiat.* **29** 409–23
Fernandez-Palomo C, Fazzari J, Trappetti V, Smyth L, Janka H, Laissue J and Djonov V 2020 Animal models in microbeam radiation therapy: a scoping review *Cancers* **12** 527
Fournier P *et al* 2017 X-Tream dosimetry of highly brilliant x-ray microbeams in the mrt hutch of the Australian synchrotron *Radiat. Meas.* **106** 405–11
Fournier P, Crosbie J C, Cornelius I, Berkvens P, Donzelli M, Clavel A H, Rosenfeld A B, Petasecca M, Lerch M L F and Bräuer-Krisch E 2016 Absorbed dose-to-water protocol applied to synchrotron-generated x-rays at very high dose rates *Phys. Med. Biol.* **61** N349
Friedl A A, Prise K M, Butterworth K T, Montay-Gruel P and Favaudon V 2021 Radiobiology of the FLASH effect *Med. Phys.* **49** 1993–2013
Fukunaga H, Butterworth K T, McMahon S J and Prise K M 2021 A brief overview of the preclinical and clinical radiobiology of microbeam radiotherapy *Clin. Oncol.* **33** 705–12
Gaide O *et al* 2022 Comparison of ultra-high versus conventional dose rate radiotherapy in a patient with cutaneous lymphoma *Radiother. Oncol.* **174** 87–91
International Atomic Energy Agency 2017 Dosimetry of small static fields used in external beam radiotherapy. An IAEA/AAPM international code of practice for reference and relative dose determination *Technical Report Series No.* 483 (International Atomic Energy Agency)
International Atomic Energy Agency 2024 Absorbed dose determination in external beam radiotherapy (Rev. 1) *Technical Report Series No.* 398 (International Atomic Energy Agency)
Joint Committee for Guides in Metrology 2004 *Guide to the Expression of Uncertainty in Measurement (GUM). Technical Report BIPM:100* (International Organization for Standardization, Sevres-BIPM)
Kaveckyte V, Persson L, Malusek A, Benmakhlouf H, Carlsson G A and Carlsson Tedgren Å 2020 Investigation of a synthetic diamond detector response in kilovoltage photon beams *Med. Phys.* **47** 1268–79
Laissue J A *et al* 2001 Weanling piglet cerebellum: a surrogate for tolerance to MRT (microbeam radiation therapy) in pediatric neuro-oncology *Proc. SPIE* **4508** 65–73
Lerch M L F, Petasecca M, Cullen A, Hamad A, Requardt H, Bräuer-Krisch E, Bravin A, Perevertaylo V L and Rosenfeld A B 2011 Dosimetry of intensive synchrotron microbeams *Radiat. Meas.* **46** 1560–5
Lienert U, Gutschmidt S, Bäcker T, Hegedüs Z, and Müller T 2024 Swedish Materials Science beamline (SMS) at PETRA III: in-line branch (P21.2) (available at: https://photon-science.desy.de/sites/site_photonscience/content/e58/e176720/e177229/e320573/e320670/infoboxContent320671/P212_beamline_poster_eng.pdf) (Accessed December 2024)
Livingstone J, Stevenson A, Butler D, Hausermann D and Adam J-F 2016 Characterization of a synthetic single crystal diamond detector for dosimetry in spatially fractionated synchrotron x-ray fields *Med. Phys.* **43** 4283–93
Lye J E, Harty P D, Butler D J, Crosbie J C, Livingstone J, Poole C M, Ramanathan G, Wright T and Stevenson A W 2016 Absolute dosimetry on a dynamically scanned sample for synchrotron radiotherapy using graphite calorimetry and ionization chambers *Phys. Med. Biol.* **61** 4201
Ma C-M, Coffey C W, DeWerd L A, Liu C, Nath R, Seltzer S M and Seuntjens J P 2001 AAPM protocol for 40–300 kV x-ray beam dosimetry in radiotherapy and radiobiology *Med. Phys.* **28** 868–93
Ortiz R, De Marzi L and Prezado Y 2022 Preclinical dosimetry in proton minibeam radiation therapy: robustness analysis and guidelines *Med. Phys.* **49** 5551–61
Petasecca M *et al* 2012 X-Tream: a novel dosimetry system for synchrotron microbeam radiation therapy *J. Instrum.* **7** 07022
Prezado Y, Vautrin M, Martínez-Rovira I, Bravin A, Estève F, Elleaume H, Berkvens P and Adam J F 2011 Dosimetry protocol for the forthcoming clinical trials in synchrotron stereotactic radiation therapy (SSRT) *Med. Phys.* **38** 1709–17
Priyadarshika R C U, Crosbie J C, Kumar B and Rogers P A W 2011 Biodosimetric quantification of short-term synchrotron microbeam versus broad-beam radiation damage to mouse skin using a dermatopathological scoring system *Br. J. Radiol.* **84** 833–42
Schültke E *et al* 2021 A mouse model for microbeam radiation therapy of the lung *Int. J. Radiat. Oncol. Biol. Phys.* **110** 521–5
Schültke E *et al* 2022 The microbeam insert at the white beam beamline P61A at the synchrotron PETRA III/DESY: a new tool for high dose rate irradiation research *Cancers* **14** 5137
Schültke E, Balosso J, Breslin T, Cavaletti G, Djonov V, Esteve F, Grotzer M, Hildebrandt G, Valdman A and Laissue J 2017 Microbeam radiation therapy—grid therapy and beyond: a clinical perspective *Br. J. Radiol.* **90** 20170073
Smyth L M L, Senthi S, Crosbie J C and Rogers P A W 2016 The normal tissue effects of microbeam radiotherapy: what do we know and what do we need to know to plan a human clinical trial? *Int. J. Radiat. Biol.* **92** 302–11
van der Sanden B, Bräuer-Krisch E, Siegbahn E A, Ricard C, Vial J-C and Laissue J 2010 Tolerance of arteries to microplanar x-ray beams *Int. J. Radiat. Oncol. Biol. Phys.* **77** 1545–52
Vozenin M-C, Bourhis J and Durante M 2022 Towards clinical translation of FLASH radiotherapy *Nat. Rev. Clin. Oncol.* **19** 791–803
Vozenin M-C, Loo B W, Tantawi S, Maxim P G, Spitz D R, Bailat C and Limoli C L 2024 FLASH: new intersection of physics, chemistry, biology and cancer medicine *Rev. Mod. Phys.* **96** 035002
Wegner M, Frenzel T, Krause D and Gargioni E 2023 Development and characterization of modular mouse phantoms for end-to-end testing and training in radiobiology experiments *Phys. Med. Biol.* **68** 085009